Electron affinity and binding energy of excitons in disordered organic semiconductors. III. Multimethod study for films of the blue fluorescent emitter MADN

E. J. de Jong [1], N. G. de Rooij [1], W. F. M. van Geel [1], C. Hauenstein [2], H. Tomita [1], G. Tirimbò [3], M. Berghuis [4], S. Gottardi [2], B. Baumeier [3,5] and R. Coehoorn [1,5,*]

[1]*Department of Applied Physics and Science Education, Eindhoven University of Technology, P.O. Box 513, NL-5600 MB Eindhoven, The Netherlands*

[2]*Simbeyond B.V., Het Eeuwsel 57, 5612 AS Eindhoven, The Netherlands*

[3]*Department of Mathematics and Computer Science, Eindhoven University of Technology, P.O. Box 513, NL-5600 MB Eindhoven, The Netherlands*

[4]*Department of Applied Physics and Science Education, Institute for Photonic Integration, Eindhoven University of Technology, P.O. Box 513, NL-5600 MB Eindhoven, The Netherlands*

[5]*Institute for Complex Molecular Systems, Eindhoven University of Technology, P.O. Box 513, NL-5600 MB Eindhoven, The Netherlands*

(Received 21 July 2025; accepted 22 October 2025; published 4 December 2025)

A method is developed for deducing the electron affinity of disordered organic semiconductors from spectroscopic thin-film studies of the ionization energy and the optical gap energy, combined with field-induced dissociation (FID) device experiments that are analyzed with kinetic Monte Carlo simulations using a methodology that has been presented by de Jong *et al.*, Phys. Rev. B **112**, 224202 (2025). The FID experiments are carried out for a set of eight organic semiconductor materials that are often used in organic light-emitting diodes. The analysis is focused on the α and β isomers of the blue fluorescent emitter material 2-methyl-9,10-di-naphthyl-anthracene. For these two materials, the experimental ionization energy, the optical gap energy, the exciton binding energy, and the electron affinity are shown to be consistent with the results of quantum-chemical calculations, presented by G. Tirimbò *et al.*, Phys. Rev. B **112**, 224203 (2025). For all fluorescent emitter materials studied, the FID experiments reveal an exciton binding energy of approximately 1.0–1.2 eV, whereas for a thermally activated delayed fluorescence material, a slightly smaller value is obtained.

DOI: 10.1103/kcl9-54vq

I. INTRODUCTION

This is the third in a series of papers in which we explore theoretical and simulation-assisted experimental methods for deducing the electron affinity and exciton binding energy in disordered small-molecule organic semiconductors with an accuracy of 0.1 eV or better. As discussed in the Introduction of the first paper (paper I, Ref. [1]), attaining the electron affinity with such an accuracy from experiments is a challenging goal due to the effects of energetic disorder, the large exciton binding energies, and the need to correct for various complicating effects when analyzing the results of spectroscopic experiments such as inverse photoelectron spectroscopy (IPES [2–4]) or low-energy inverse photoelectron spectroscopy (LEIPS [5–7]). From an analysis of results of three-dimensional kinetic Monte Carlo (3D-KMC) simulations, paper I concludes that it should be feasible to deduce the singlet exciton binding energy $E_{S,b}$ with an accuracy of 0.1–0.15 eV, using field-induced dissociation (FID) experiments. The electron affinity E_{EA} would then follow from the fundamental relation

$$E_{EA} = E_{IE} - E_S - E_{S,b}, \tag{1}$$

with E_{IE} the experimental ionization energy and E_S the experimental singlet exciton energy. All quantities that enter Eq. (1) are defined as the disorder-averaged adiabatic bulk values.

In the second paper (paper II, Ref. [8]), a full theoretical toolchain is presented from which, for a thin film with a realistic morphology, all energies that enter Eq. (1), their distributions, and their correlations can be deduced. The methodology was demonstrated for the two (α and β) isomers of the prototypical material 2-methyl-9,10-di-naphthyl-anthracene (MADN), which have been used as an ambipolar host in the emissive layer of deep-blue fluorescent organic light-emitting diodes (OLEDs) [9–16]. The structure of the two isomers is shown in Figs. 1(a) and 1(b). We regard MADN as particularly suitable for studies of the electronic structure and excitonic states of disordered organic semiconductors because the frontier orbital states, which are located on the anthracene core, are nondegenerate. As shown in Ref. [17] and in paper II [8], that facilitates the analysis of ultraviolet photoelectron spectroscopy (UPS) and LEIPS spectra. Furthermore, MADN films are morphologically stable, with a glass temperature of 120 °C [14], as the methyl

*Contact author: r.coehoorn@tue.nl

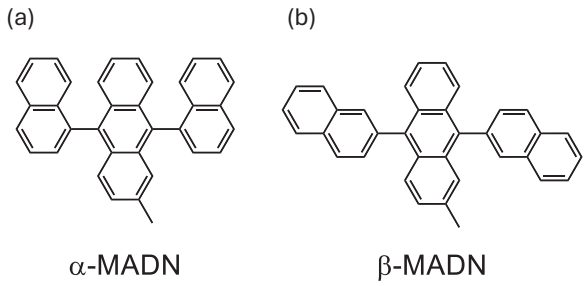

FIG. 1. Molecular structures of (a) α-MADN and (b) β-MADN. In the neutral ground state, the dihedral angle between the naphthyl side groups and the anthracene core is for both isomers equal to 90° (see Fig. S1 of Ref. [8]).

substituent disrupts the symmetry and stabilizes the material against crystallization. A comparison of results for both isomers elucidates the subtle effects of delocalization of the frontier orbital and exciton states due to rotations of the anthracene-naphthyl dihedral angles. Such rotations are easier for β-MADN.

The purpose of this third paper is to study the extent to which the electron affinity of the two isomers of MADN can be accurately obtained using a multimethod approach that is based on Eq. (1) and combines results from UPS, optical spectroscopy, and FID experiments for obtaining E_{IE}, E_{S}, and $E_{\mathrm{S,b}}$, respectively. We use the results of UPS experiments that were already presented in Ref. [17]. In this paper, E_{S} is determined from an analysis of optical absorption and emission spectra of solutions, neat films, and blends, and $E_{\mathrm{S,b}}$ is determined from an analysis of the results of FID experiments using kinetic Monte Carlo simulations, so that the sensitivity of various complicating effects is clarified. In order be able to discuss the FID results from a broader perspective, we also present FID results for neat films of six other disordered organic semiconductor materials that are frequently used in OLEDs. The values of the electron affinities of the two isomers of MADN that follow from these studies using Eq. (1) are compared with results of an analysis of LEIPS experiments that was given in paper II [8]. Figure 2 gives a schematic view of the methods that are combined in this work.

The structure of the paper is as follows. In order to make the paper sufficiently self-contained, Sec. II contains a brief summary of the results of quantum-chemical studies for the two isomers of MADN that were presented in paper II [8]. In Sec. III, we present measured absorption and emission (photoluminescence, PL) spectra for neat and blended thin films and of solutions of both isomers, measured PL efficiencies of thin films, and Franck-Condon analyses of the spectra that lead to E_{S}. In Sec. IV, we give the results of FID experiments for eight small-molecule materials, including α-MADN and β-MADN. 3D-KMC simulations are used for deducing the exciton binding energy, following the methodology that was developed in paper I [1]. Sensitivity analyses are carried out to determine the uncertainty to various material parameters. In Sec. V, a summary, conclusions, and outlook are given.

II. PREVIOUS WORK

In Ref. [17] and in paper II [8], results of first-principles calculations of the electronic structure and excitonics of thin films of α-MADN and β-MADN have been presented, using quantum-chemical theory that includes quasiparticle corrections within the *GW* approximation of many-body Green's function theory and using the Bethe-Salpeter equation. The thin film and vacuum surface morphology have been obtained from deposition simulations, for a system containing of the order of 500–1000 molecules. This extended toolchain involves a significant computational effort using today's computational resources. The *GW* calculations include the electronic polarizability of the molecules within a radius of 6 nm and provide the vertical lowest unoccupied molecular orbital (LUMO) energies for all molecules in the structurally disordered thin-film system. The conformational, positional, and orientational disorder are thus taken into account.

For both isomers of MADN, a small net orientation of the static molecular dipole moments was found to give rise to a gradient of the vertical ionization energy and electron affinity across the film thickness. The finally used values

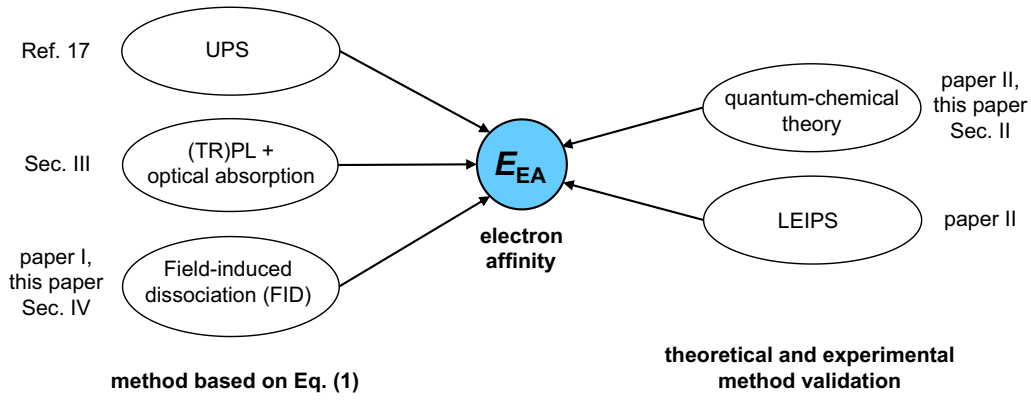

FIG. 2. Schematic view of the method that is employed in this work for obtaining the electron affinity E_{EA} of α-MADN and β-MADN (left part of the figure). The results are compared to the result of quantum-chemical theory and LEIPS experiments (right part of the figure). Quantum-chemical theory is also used to support the analysis of UPS, optical, and LEIPS experiments. Conversely, the finding of a consistent set of experimental electronic and excitonic energies allows validating the quantum-chemical methodology. Papers I and II are Refs. [1] and [8], respectively.

TABLE I. Overview of the results from quantum-chemical studies for thin films of α-MADN and β-MADN, obtained in Ref. [17] and paper II [8]. The mean adiabatic bulk values of the ionization energy (E_{IE}) and the electron affinity (E_{EA}) have been obtained by extrapolation of the bulk highest occupied molecular orbital (HOMO) and LUMO energies, respectively, to the vacuum interface. The singlet binding energy ($E_{S,b}$) has been obtained using $E_{S,b} \equiv E_{gap} - E_S$, with E_S the singlet energy and E_{gap} the gap energy that is obtained directly from the differences between the HOMO and LUMO energies in the bulk of the film ("direct method", explained in Sec. II). By avoiding extrapolation to the vacuum surface, this value is expected to be more accurate than the difference between the extrapolated energies E_{IE} and E_{EA}. The table also contains the corresponding disorder energies σ (standard deviation of the distribution) and the corresponding reorganization energies λ_{reorg} due to intramolecular structural relaxation. The uncertainties (standard deviations) of the mean values are given in parentheses. The values of E_{IE} have been obtained in Ref. [17]. All other values have been taken from paper II [8].

Energies (eV)	E_{IE}	E_{EA}	E_{gap}	E_S	$E_{S,b}$
α-MADN					
Mean	5.91	1.83	3.98	2.96	1.02
	(0.05)	(0.13)	(0.11)	(0.04)	(0.11)
σ	0.10	0.14		0.04	0.14
λ_{reorg}	0.21	0.23		0.20	
β-MADN					
Mean	5.89	1.83	4.00	2.90	1.10
	(0.05)	(0.14)	(0.13)	(0.04)	(0.12)
σ	0.13	0.19		0.04	0.15
λ_{reorg}	0.21	0.19		0.21	

were obtained by extrapolating these calculated values to the surface planes. The adiabatic ionization energies and electron affinities are obtained from these vertical energies by taking the effect of a reorganization energy λ_{reorg} due to structural relaxation of the molecule on which the electron (e), hole (h), or singlet exciton (S) resides into account: $E_{IE} = E_{IE,vert} - \lambda_{reorg,h}$, $E_{EA} = E_{EA,vert} + \lambda_{reorg,e}$. Also for calculating the adiabatic singlet energy, this reorganization energy correction is made: $E_S = E_{S,vert} - \lambda_{reorg,S}$. In principle, the gap energy $E_{gap} \equiv E_{IE} - E_{EA}$ can be obtained using the vertical energies that follow from the extrapolation procedure that has been outlined above. However, it was found in paper II [8] that the statistical uncertainty in the gap energies can be reduced by making use of the directly calculated distribution of gap energies across the film thickness. This direct method has been used to derive the gap energies and the exciton binding energies that are given in Table I, which summarizes the theoretical results from paper II [8], including the distribution widths of all quantities and the reorganization energies.

The values of E_{IE} that are given in Table I have been validated in Ref. [17] by the finding that for both isomers of MADN, the onset energies of the measured and predicted UPS spectra agree excellently (within 0.02 eV). A similar comparison in paper II [8] between the onset energies of the measured and predicted LEIPS spectra, which probe E_{EA}, revealed a difference of about 0.2 eV. This difference is still within the uncertainty margins of the experimental and theoretical methodologies. From a comparison in paper II [8] and in Sec. III of this paper, the predicted values of E_S are shown to agree excellently with experiment, viz. within about 0.05 eV.

The gap energies for α-MADN and β-MADN are very similar, viz. 3.98 ±0.11 eV and 4.00 ±0.13 eV, respectively. That may be explained from the similar shape of the frontier orbital wave functions, which for both molecules are localized on the anthracene core of the molecule (see Fig. S1 of the Supplemental Material of paper II in [8]). However, the disorder energies are found to be much larger for β-MADN than for α-MADN. A plausible explanation is the smaller energy barrier for dihedral angle rotations around the naphthyl-anthracene bonds in β-MADN, away from the gas-phase equilibrium angle of 90°, leading to more orbital delocalization to the naphthyl side groups and an enhanced sensitivity of E_{IE} and E_{EA} to structural disorder.

III. OPTICAL SPECTROSCOPY

A. Optical absorption and emission experiments

The adiabatic singlet energy can be deduced from results of optical absorption and emission (photoluminescence, PL) experiments, as will be discussed in Sec. III C. Even though the results of such studies have been reported in earlier works [12,13,18–24], this has not yet provided a systematic view of the sensitivity of the spectra to the measurement conditions. We have therefore measured for both isomers of MADN absorption and emission spectra of dilute (8 μM) solutions in dichloromethane (DCM) and of neat ∼90 nm thin films, fabricated by spin coating on glass from solutions in DCM and by evaporation deposition. The PL spectra were obtained after excitation by a 380 nm emission wavelength source. The solution spectra were obtained using a small solute concentration in order to avoid interaction effects and a resulting spectral broadening occurring at larger concentrations. In addition, PL spectra of 150 nm films on quartz of 5 mol% blends of both isomers in the ultrahigh gap host material 1,4-bis(triphenylsilyl)benzene (UGH2) have also been studied. This matrix material, with a singlet energy of 4.4 eV [25] and a HOMO energy of −7.2 eV (onset value) [26], provides excellent exciton confinement.

Before presenting the experimental results, we first remark that a proper comparison of absorption and PL spectra requires representing them on an energy scale and transforming them into normalized distributions $W_A(E) \propto I_A(E)/E$ and $W_{PL}(E) \propto I_{PL}(E)/E^3$, respectively. When the vibronic effects on the absorbance and PL spectra are well described within Franck-Condon theory, these distributions are equal to the distributions of the squared densities of the coupled electronic-vibronic transition dipole moments for absorption and emission [27].

Figure 3 shows a comparison of such energy-corrected spectra, for the solutions [Fig. 3(a) and 3(b)] and the solution-processed or evaporation deposited films [Figs. 3(c) and 3(d)] of the two isomers. The full and dashed black curves show the normalized $W_A(E)$ curves and their mirror images. The mirror-imaged curves were redshifted such that their peak structure coincides optimally with the peak structure of the experimental normalized $W_{PL}(E)$ curves for the same systems

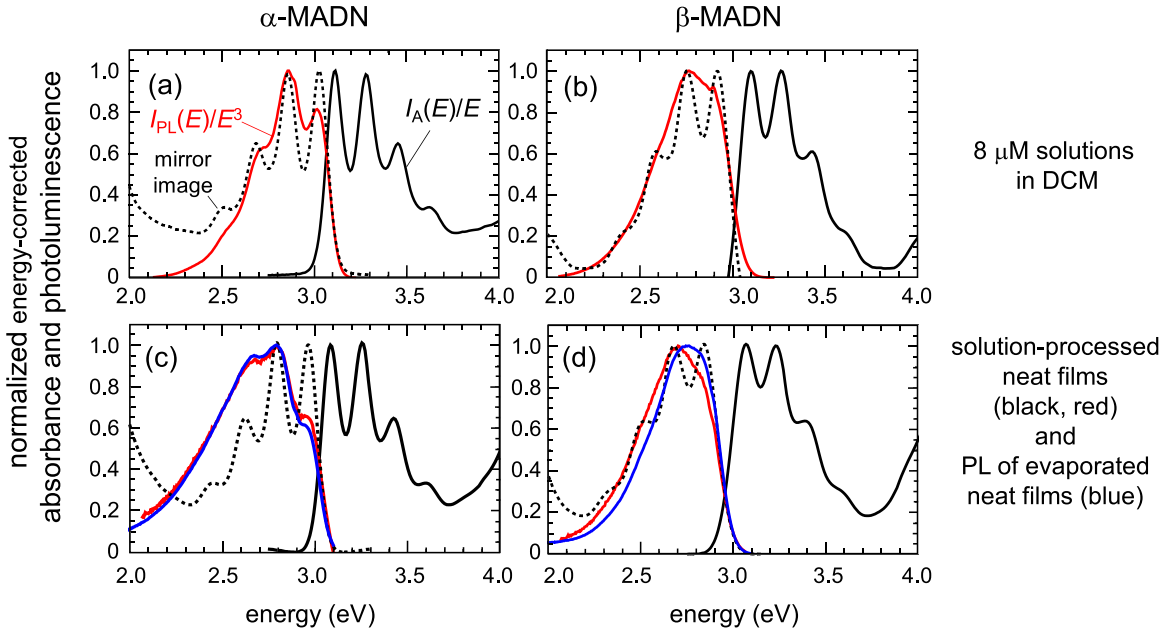

FIG. 3. Normalized energy-corrected absorbance and photoluminescence (a),(b) for 8 μM solutions in DCM and (c),(d) for thin films, for α-MADN and β-MADN, respectively.

(full red curves). All absorption spectra show an increase due to higher-energy absorption for energies above 3.75 eV. For energies far from the leading edge, a good comparison of the measured PL spectra with the mirror-imaged absorption spectra is therefore not possible. Figure S1 of the Supplemental Material [28] gives an overview of the measured wavelength-dependent absorption spectra, in absolute units, and the normalized PL spectra. Figure S2 of the Supplemental Material [28] shows the sensitivity of the absorption spectra of solutions to the solute concentration.

The absorption spectra for solutions of α-MADN and β-MADN show a clear vibronic progression. The effect is most pronounced for α-MADN. The PL spectra for solutions are not quite mirror symmetric with the absorption spectra, but show some peak broadening and a decrease of the relative intensity of the highest-energy peak for both isomers. A possible cause of this effect will be discussed in Sec. III C. The thin-film results show similar general trends. For all spectra, the vibronic progression is somewhat less well defined, the leading absorption and PL peak energies are redshifted, and the PL spectra are significantly broadened, in particular for α-MADN. Interestingly, the PL spectra for α-MADN show a significant broadening and redshift, both for the solution-processed and evaporated films. For the β-MADN films, these effects are much smaller. This result might seem paradoxical, as the absorption spectra suggest that for α-MADN, inhomogeneous line broadening due to energetic disorder is smaller than for β-MADN. We ascribe the effect to exciton relaxation, resulting from Föster-type transfer in the Gaussian exciton density of states (DOS), in combination with an aggregation-induced redshift. The effect is apparently stronger for α-MADN than for β-MADN.

A comparison of measured PL spectra for neat films and 5 mol% blends in UGH2, shown in Fig. 4, supports that view: preventing exciton diffusion by embedding in a UGH2 matrix strongly reduces the spectral broadening to low energies, in particular for α-MADN. The effects of spectral broadening and redshift due to exciton relaxation are discussed in more depth in Sec. III C.

B. PLQE measurements and time-resolved PL experiments

Time-resolved PL (TRPL) experiments and PL quantum efficiency (PLQE, η_{PL}) measurements were carried out to obtain additional information on the effects of exciton diffusion on the PL spectra. Section S3 of the Supplemental Material [28] contains a description of the experimental methods that were used and Fig. S3 in the Supplemental Material [28] shows the TRPL data for the solutions in DCM and for the solution-processed films. Table II gives an overview of the measured PLQEs and effective emissive lifetimes.

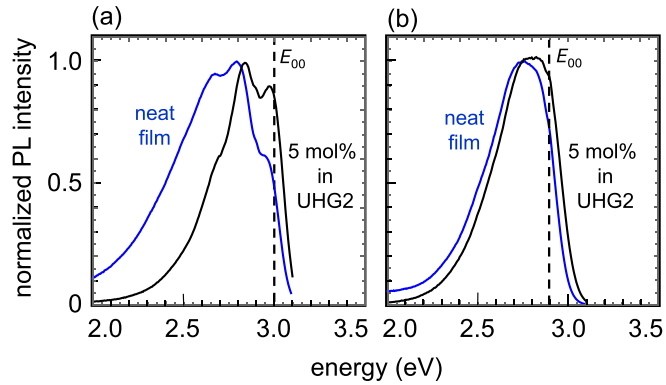

FIG. 4. Photoluminescence (PL) spectra of 150 nm evaporation-deposited films on quartz of (a) α-MADN and (b) β-MADN, for neat films and 5 mol% blends in UGH2.

TABLE II. Results of PLQE and time-resolved PL experiments for 8 μM solutions in DCM, solution-processed, and ∼90 nm evaporation-deposited neat films and evaporation-deposited blend films (5 mol% in UGH2). When the time-resolved PL shows mono-exponential decay, the emissive lifetime τ is given. When nonexponential decay of the form $\sum_{i=1}^{i_{max}} A_i \exp(-t/\tau_i)$ is observed, the lifetimes τ_i are given as well as the normalized weights $A_i\tau_i/(\sum_{i=1}^{i_{max}} A_i\tau_i)$, expressed in percents.

	α-MADN		β-MADN	
System	τ_i (ns)	η_{PL}(%)	τ_i (ns)	η_{PL}(%)
Solution in DCM	5.5		3.6	
Neat film (sol.)	0.46 (68%)		0.80 (83%)	
	1.8 (25%)		1.9 (17%)	
	6.7 (7%)			
Neat film (evap.)	0.44 (18%)	3.3	0.53 (56%)	3.2
	1.6 (21%)		1.4 (32%)	
	7.5 (61%)		6.9 (12%)	
Blend film (UGH2)	5.5	40	3.8	40

For solutions in DCM and for evaporation-deposited dilute films of MADN in UGH2, the emission shows a close to mono-exponential decrease. The effective lifetimes were found to be almost equal, viz. ∼5.5 ns for dilute α-MADN systems and ∼3.7 ns for dilute β-MADN systems. These values are similar to those for dilute solutions of anthracene in cyclohexane ($\tau_{eff} = 4.9$ ns [29]) and for dilute solutions of various 9,10-diphenylanthracene-based molecules in tetrahydrofuran (THF) [30].

In contrast, the TRPL intensity of solution-processed and evaporation-deposited neat films shows a multiexponential decrease. Three-component fits to the shapes are given in the footnotes of Table II. The initial intensity decrease is much faster than that found for dilute systems. Consistent with this observation, η_{PL} is in a UGH2 thin-film matrix for both isomers equal to 0.40, whereas η_{PL} is only about 0.03 for the neat evaporation-deposited films. Such a large difference was also observed when comparing dilute and neat films of various 9,10-diphenylanthracene-based molecules [30]. The effect was ascribed by the authors to the occurrence of loss processes as a result of exciton diffusion to quenching sites, such as intrinsic or extrinsic defects. Also, for the MADN films, such a concentration quenching effect would provide a plausible explanation for the small PLQE of thin films. The quenching could be explained as a result of low-efficiency emission from aggregates or of quenching at extrinsic defects.

C. Analysis

For obtaining the electron affinity using Eq. (1), we need to determine E_S, the adiabatic energy of singlet excitons in a thin-film material. We deduce E_S from the zero-vibrational (0-0) leading-edge peaks in the measured thin-film absorption and emission spectra, $E_{0-0,A}$ and $E_{0-0,PL}$, respectively, using [31]

$$E_S = \tfrac{1}{2}(E_{0-0,A} + E_{0-0,PL}). \quad (2)$$

Qualitatively, the difference between E_S, $E_{0-0,PL}$, and $E_{0-0,A}$ can be understood as follows. On the one hand, E_S is smaller than $E_{0-0,A}$, as after an optical excitation process, slow vibrational or orientational relaxation of molecules surrounding a singlet-excited molecule lead to a stabilization of the singlet state. On the other hand, the system is immediately after radiative decay not yet in the ground state, as the polarization cloud is still present, so that E_S is larger than $E_{0-0,PL}$. Equation (2) expresses that the reduction of the total energy of the system due to the creation of the exciton-induced polarization cloud in the environment of the molecule is a self-energy: it is equal to half of the energy that would be needed to fully separate the exciton from the induced polarization cloud (while leaving that polarization cloud intact). The difference between the 0-0 energies for absorption and emission quantifies this relaxation effect and is often defined as the Stokes shift, ΔE_{Stokes}.

Deriving $E_{0-0,A}$ and $E_{0-0,PL}$ from the spectra of thin films can be complicated by (i) strong coupling to multiple high-energy vibronic modes, leading to relatively weak 0-0 transitions, (ii) coupling to modes with energies below the thermal energy, effectively leading to Gaussian broadening of the vibronic peak structure [32], and (iii) a redshift of the emission spectra due to diffusion-induced relaxation in the exciton density of states (DOS). Full excition relaxation in a Gaussian exciton DOS is expected to lead to a shape-conserving shift of the PL spectrum by an energy $\sigma_{exc}^2/(k_B T)$ (the thermal equilibrium energy; see, e.g., Ref. [33]), which is about 0.06 eV for the two isomers of MADN when taking $\sigma_{exc} = 0.04$ eV from paper II [8]. For neat films of α-MADN, the redshift [see Fig. 3(c)] with respect to the spectra of solutions [Fig. 3(a)] and blend systems [Fig. 4(a)] is larger than expected from the analysis given above, and not shape conserving. We attribute that to the relaxation to partially emissive low-energy defect states such as aggregates. For β-MADN, the shift is about 0.05 eV, i.e., close to the expected value and more shape conserving. The shape of PL spectra of neat films could furthermore be affected by the effects of strong exciton quenching, discussed in Sec. III B. We will therefore use the PL spectra of the 5 mol% blends in UGH2 for obtaining $E_{0-0,PL}$.

Table III gives an overview of the results of multimode Franck-Condon analyses of the measured absorption and emission spectra. Within such an analysis, the PL spectrum is described as a sum of Gaussian-broadened contributions due to emission involving the simultaneous creation of $\{m_1, m_2, \ldots, m_N\}$ vibrations of mode i, with m_i a non-negative integer [34],

$$W_{PL}(E) \propto \sum_{m_1=0}^{\infty}\sum_{m_2=0}^{\infty}\cdots\sum_{m_N=0}^{\infty}\left\{\left[\prod_{i=1}^{N}\frac{S_i^{m_i}\exp(-S_i)}{m_i!}\right] \times \frac{1}{\sqrt{2\pi\sigma_{eff}^2}}\exp\left[-\frac{(E - E_{0-0,PL} + \sum_i m_i\hbar\omega_i)^2}{2\sigma_{eff}^2}\right]\right\}, \quad (3)$$

with $\hbar\omega_i$ the energy of vibrational mode i, S_i the dimensionless coupling strength (Huang-Rhys factor) to mode i, and σ_{eff} the effective Gaussian peak width (standard deviation). An analogous expression is used for describing the absorption spectrum. For both isomers, fair fits are already obtained

TABLE III. Results of Franck-Condon analyses [Eqs. (3)–(5)] of the absorption and PL spectra of α-MADN and β-MADN solutions, neat thin films, and 5 mol% blends in UGH2, shown in Figs. 3 and 4. Such analyses lead to a 0-0 vibrational peak energy, E_{0-0}, a total reorganization energy due to coupling with high-energy vibrational modes, λ_{high} [defined in Eq. (5)], and an effective peak width σ_{eff} due to coupling to low-energy modes and thermal excitations [see Eq. (4)]. The final results of this study are the adiabatic singlet energies for neat thin-film systems (italicized font). These have been obtained by combining the 0-0 peak energies from the neat film absorption spectra with the 0-0 peak energies of the blend film PL spectra. Their experimental uncertainty is approximately ±0.03 eV. The quality of the fits to the PL spectra of the blend systems is shown in Sec. S4 of the Supplemental Material [28].

	Absorption			Photoluminescence			
	E_{0-0} (eV)	λ_{high} (eV)	σ_{eff} (eV)	E_{0-0} (eV)	λ_{high} (eV)	σ_{eff} (eV)	E_S (eV)
Solutions							
α-MADN	3.11	0.19	0.046	3.04	0.22	0.05	3.07
β-MADN	3.10	0.180	0.062	2.95	0.22	0.07	3.02
Neat films							
α-MADN	3.08	0.19	0.051				*3.04*
β-MADN	3.06	0.18	0.064				*2.98*
Blends							
α-MADN				2.99	0.19	0.06	
β-MADN				2.89	0.17	0.07	

assuming a single mode, with an energy of about 0.16 eV, which corresponds to the C-C stretch modes in the anthracene cores of the molecules. Adding a second mode improves the fits only slightly. As an example, the fit results for the 5 mol% blend systems are shown in Sec. S4 of the Supplemental Material [28]. We note that performing accurate Franck-Condon analyses of the absorption spectra is hampered by the contributions due to higher-energy absorption, above 3.75 eV. However, the resulting uncertainty of the 0-0 peak energies is found to be very small.

Using Eq. (2), the adiabatic singlet energies are found to be 3.07 ± 0.02 eV and 3.02 ±0.02 eV for α-MADN and β-MADN solutions, respectively, and 3.04 ± 0.02 eV and 2.98 ± 0.04 eV for α-MADN and β-MADN thin films, respectively. The thin-film results have been obtained using $E_{0-0,A}$ from neat films and $E_{0-0,PL}$ from the blend systems. These experimental thin-film values agree excellently, within the small experimental and theoretical uncertainty ranges, with the results from the quantum-chemical calculations, given in Table I. For β-MADN, the optical gap is, from both approaches, found to be a few hundredths of an eV smaller than for α-MADN.

A slightly larger uncertainty has been given to the adiabatic singlet energy of films of β-MADN, for which the PL spectrum has a less well-resolved vibronic structure. In the fits, that leads to larger values of the Gaussian peak widths. Two-mode fits of the PL spectra of the blend systems yield $\sigma_{eff} = 0.060$ eV and 0.074 eV for α-MADN and β-MADN, respectively. The peak width is due to a Marcus-type coupling with vibrational modes with energies below the thermal energy and due to the inhomogeneous Gaussian disorder σ_{exc} of the exciton energies,

$$\sigma_{eff} = \sqrt{2\lambda_{low}\frac{k_B T}{e} + \sigma_{exc}^2}, \tag{4}$$

with λ_{low} the reorganization energy due to coupling with all low-energy modes of the excited molecule, k_B the Boltzmann constant, and T the temperature. A derivation of the contribution from the low-energy modes [first term under the square-root sign in Eq. (4)] has been given, for example, in Appendix A of Ref. [32]. The derivation is based on a summation such as given in Eq. (3) over all modes, after including temperature- and mode-energy-dependent proportionality factors that are determined by the probability that a certain number of vibrational modes of a certain type has been thermally excited, and after replacing, in Eq. (3), σ_{eff} by σ_{exc}.

Equation (4) can be used to estimate λ_{low} for the thin films of 5 mol% $\alpha(\beta)$-MADN in UGH2. The observed values of σ_{eff} of about 0.060 (0.074) eV and the theoretical values of σ_{exc} of 0.04 (0.04) eV that were obtained in paper II [8] (for neat films) would lead to $\lambda_{low} \approx 0.04$ (0.08) eV. The larger value for β-MADN is most likely related to the more delocalized nature of the exciton wave functions: whereas excitons on α-MADN are strongly localized on the anthracene cores, they are slightly delocalized to the naphthyl side groups for β-MADN (see paper II [8]). The singlet-exciton energies in β-MADN are therefore more sensitive to variations of the dihedral angles of the core-ligand bonds and to polarizability fluctuations of the thin-film environment.

The total singlet-exciton reorganization energies for thin films of α-MADN and β-MADN that follow from the Franck-Condon analysis of the PL spectra of the blend systems,

$$\lambda_{tot} \equiv \lambda_{low} + \lambda_{high} = \lambda_{low} + \sum_i S_i \hbar\omega_i, \tag{5}$$

are approximately 0.23 and 0.24 eV, respectively. These results are both close to the values of 0.20 and 0.21 eV, respectively, that were obtained in paper II [8] from quantum-chemical calculations for neat films. We note that the effective disorder energy for embedding in UGH2 might be slightly different than for embedding in a neat film.

The Stokes shifts that are obtained from the solution spectra or from the absorption spectra for neat films combined with the PL spectra for the blend films are about 0.09 and 0.17 eV, for α-MADN and β-MADN, respectively. We speculate that the larger Stokes shift for β-MADN is due to the more extended nature of the electronic and excitonic states on that isomer. Combined with the flexibility of the core-ligand dihedral bonds, a stronger vibrational response of the molecules in the immediate environment of a singlet is then expected.

The W_{PL} and W_A spectra are for none of the systems studied in Fig. 3 precisely mirror symmetric. Whereas the deviations that are found for neat films [Figs. 3(c) and 3(d)] can be explained, at least in part, as a result of diffusion-induced relaxation in the exciton DOS, such an explanation cannot be given for dilute solutions [Figs. 3(a) and 3(b)]. The absence of mirror symmetry indicates that the coupling with at least one relevant mode is not well described within the Franck-Condon picture, which assumes excitation and deexcitation between

two single-well harmonic potentials that are displaced along a certain reaction coordinate. A more complex situation can arise when the excited-state potential has the form of a double well, e.g., due to two equivalent energy minima at torsional angles that deviate equal amounts from a 90 degree configuration. As shown in Ref. [35], the PL spectrum could then be more strongly broadened than the absorption spectrum, similar to our experimental findings. Reversely, when the ground-state potential has the form of a double well, the absorption spectrum can be more strongly broadened than the PL spectrum [36]. For the two isomers of MADN, within the ground state, a 90 degree rotation angle around the core-naphthyl bond axis, the ground-state potential has the form of a single well. The experimentally observed effect would be expected if, in the singlet-excited state, the equilibrium angle would deviate from 90 degrees. However, quantum-chemical calculations do not show such an effect (see paper II [8]). We cannot exclude that dynamical molecule-solvent interactions play a role.

IV. FIELD-INDUCED DISSOCIATION EXPERIMENTS

A. Experimental method

We have studied the field-induced dissociation of excitons in organic semiconductor (OS) materials using devices with a layer structure:

glass | ITO | PEDOT:PSS | OS | Al.

The PEDOT:PSS layers (65 nm) were spin coated on a 3 mm glass substrate, and covered with prepatterned 120 nm indium tin oxide (ITO) electrodes. Evaporation deposition at a rate of 0.2 nm/s and at a base pressure of 6×10^{-7} Torr was used to deposit 200 nm OS layers. Subsequently, 100 nm layers of aluminium (Al), serving as a counterelectrode, were thermally evaporated to complete the devices.

The experiments were carried out under reverse-bias conditions, with Al as the positive electrode and ITO|PEDOT:PSS as the negative electrode. For the materials studied in this work, the barrier for hole and electron injection is significantly larger than 1 eV, so that at sufficiently small voltages, the injection of charges is negligible. In order to minimize the probability of device breakdown, the bias voltage was applied in the form of 800 μs square pulses, with a repetition frequency of 10 Hz (period 100 ms).

Excitons were created by illuminating the devices through the ITO | PEDOT:PSS electrode, using a pulsed nitrogen laser (Stanford Research System, NL100, emission wavelength $\lambda =$ 337 nm, corresponding to a photon energy of 3.68 eV; pulse width about 3.5 ns). To ensure a constant voltage during the presence of excitons in the device, the laser pulses arrive precisely halfway along each voltage pulse. The active area of each device is 3×3 mm^2, and a circular aperture was used to confine the illuminated area to 1 mm^2. The time-integrated PL emission intensity and spectrum was measured by a CCD detector camera under an angle of approximately 30° with respect to the sample normal. The current through the device is measured using an oscilloscope that detects the voltage over a small series resistor. All experiments were carried out for a sufficiently small light intensity to avoid additional losses due to quenching and annihilation.

B. Materials studied

We have carried out FID experiments for α-MADN, β-MADN, and for six other small-molecule OS materials that have been frequently used in studies of organic light-emitting diodes (OLEDs). Figure 5 shows the molecular structures of the six additional materials and Table IV gives an overview of the full names of the materials that are studied in this work and an overview of various properties, obtained from the literature and from this work. NPB, TCTA, CBP, and mCP are frequently used as a hole-transporting layer or as a host in the emissive layer of OLEDs. TPBi is used as an electron-transporting material and has a relatively large molecular dipole moment ($p_{\mathrm{dip}} \approx 7$ D). As discussed in paper I [1], the resulting enlarged energetic disorder is expected to lead to easier field-induced dissociation. DMAC-TRZ is a donor-acceptor-type molecule that has been found to be an efficient cyan-green emitter in thermally activated delayed fluorescence (TADF-type) OLEDs [37,48–51]. One may expect that the exciton binding energy for donor-acceptor-type materials will tend to be somewhat smaller than that of small-molecule host and fluorescent emitter materials because of the enlarged electron-hole separation in the excitonic state.

C. Current-voltage characteristics and capacitance

In order to assure that under reverse-bias conditions the current density and the corresponding polaron densities are sufficiently small, so that exciton-polaron quenching does not contribute to the efficiency loss, we have first studied the current-voltage [$J(V)$] characteristics under dark conditions. All studies that are reported in this work were carried out at room temperature. As shown in Fig. S5 in Sec. S5 of the Supplemental Material [28], the $J(V)$ curves are strongly asymmetric for materials with a relatively shallow highest occupied molecular orbital (HOMO) energy (NPB, TCTA, α-MADN and β-MADN; see Table IV for a literature overview) and provide evidence for strong hole injection around and above the built-in voltage of about 1 V. Somewhat surprisingly, no strong hole injection is found for the DMAC-TRZ devices. Also for the other materials, for which the hole-injection barrier is larger, the $J(V)$ curves are quite symmetric and show no evidence of hole injection. The effective work function of the Al electrode is about 1 eV smaller than that of the ITO|PEDOT:PSS electrode, so that under reverse-bias conditions, no hole injection is expected. Experiments under reverse-bias conditions reveal indeed for most devices only a relatively small current density that increases approximately linearly from $\sim$0.02 A/m^2 at -5 V to $\sim$0.2 A/m^2 at -50 V (see Fig. S6 of the Supplemental Material [28]). We view this as a leakage current density, possibly resulting from extrinsic defect conduction. These current densities are at least two orders of magnitude smaller than the current densities that are required to induce a significant loss due to exciton-polaron quenching in fluorescent OLEDs (see, e.g., Ref. [52]). For some devices, the experiments also show dielectric breakdown already above a reverse-bias voltage of 50 V (see Fig. S6 in Sec. S5 of the Supplemental Material [28]). Even though breakdown is a stochastic process, so that studying a large set of nominally identical devices can provide useful data up to reverse-bias voltages that are larger than the average value, we

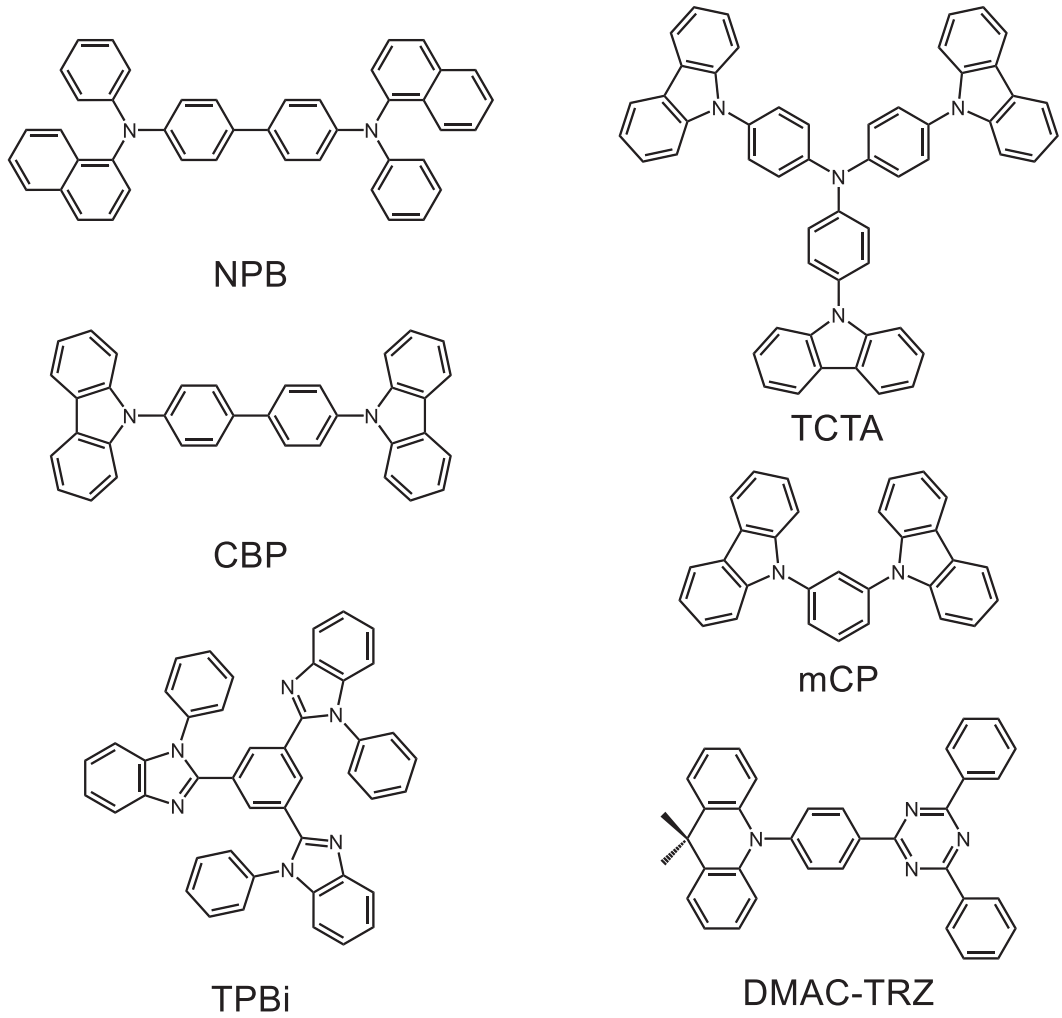

FIG. 5. Molecular structures of the materials for which FID experiments have been carried out, in addition to the materials α-MADN and β-MADN for which the structures are shown in Fig. 1.

have chosen to minimize the risk of breakdown by carrying out the FID experiments under pulsed voltage conditions, as discussed in Sec. IV A, and to limit the reverse bias voltage to 50 V.

The reliability of the experimental procedures has been further investigated by measuring, for NPB devices with thicknesses in the range 100–300 nm, the capacitance under reverse- and forward-bias conditions. Such experiments could, in particular, reveal systematic and random variations of the layer thickness, which would directly translate into an error in the field that is required to obtain a certain level of dissociation and therefore in the experimental value of $E_{S,b}$. Figures S7 and S8 in Sec. S6 of the Supplemental Material [28] show that for all layer thicknesses studied, the capacitance is voltage independent under reverse-bias conditions. The capacitance is almost frequency independent above a frequency of 10^4 Hz that is inversely proportional to the measured layer thickness. We interpret that value as the geometrical capacitance of the organic semiconductor layer, sandwiched in between two conducting electrodes. The strong correlation between the capacitance and the layer thickness shows that for the NPB devices, the layer thickness uncertainty due to random variations is small. For the other materials, only 200 nm devices were studied. The resulting values of the static relative dielectric permittivity, ε_r, are included in Table IV, and are all in the range 3.0–3.6. For the three materials for which a comparison with the literature data is possible (taken from a recent compilation in Ref. [53]), we see differences of approximately $\pm 10\%$ in either direction. The wide spread in the literature data for some intensively investigated materials (see Ref. [53]) is indicative of a certain sensitivity to the detailed device structure, deposition conditions, or the frequency at which ε_r is defined. A comparison with the literature data can therefore presently not be used to derive a proper conclusion concerning possible systematic inaccuracies in the organic semiconductor layer thickness.

D. Results of FID experiments

Figure 6 shows the results of the field-induced dissociation experiments. The blue symbols give the measured voltage and electric field dependence of the normalized PL efficiency, $\eta_{PL}(V)$, defined as the PL efficiency with respect to the zero-voltage value. The efficiency has been obtained from spectrally resolved PL experiments, by integrating the spectral

TABLE IV. Overview of the full names of the eight materials studied in this work, the highest occupied molecular orbital (HOMO) energy, the peak (onset) energy of the PL spectra, the average static molecular dipole moment, and the static relative dielectric permittivity. The (adiabatic) ionization energies E_{IE} of the two isomers of MADN are given in Table I and the (adiabatic) singlet energies E_S are given in Table III.

Material	$E_{HOMO,UPS,o}$ (eV)[a]	$E_{PL,p}$ ($E_{PL,o}$) (eV)[b]	p_{dip} (D)	ε_r [c]
α-MADN [2-methyl-9,10-di(1-naphthyl)anthracene] [d]	−5.79 [17]	2.8 (3.2)	0.59 [17]	3.20 ± 0.04
β-MADN [2-methyl-9,10-di(2-naphthyl)anthracene] [d]	−5.73 [17]	2.7 (3.1)	0.56 [17]	3.12 ± 0.05
NPB [*N,N′*-bis(naphthalen-1-yl)-*N,N′*-bis(phenyl)-benzidine]	−5.4 [38] −5.3 [40]	2.7 (3.2)	0.26 [39]	3.17 ± 0.04
TCTA [tris(4-carbazoyl-9-ylphenyl)amine]	−5.80 [6], −5.70 [41]	3.0 (3.5)	0.01 [39]	3.21 ± 0.06
CBP [4, 4′ − *N,N′*-dicarbazole-1, 1′-biphenyl]	−6.2 [42] −6.0 [40]	3.1 (3.6)	0.00 [39]	3.24 ± 0.07
mCP [1,3-bis(*N*-carbazolyl)benzene]	−6.0 [26]	3.4 (3.6)	1.33 [39]	3.55 ± 0.03
TPBi [2, 2′, 2″-(1,3,5-benzinetriyl)-tris(1-phenyl-1-*H*-benzimidazole)]	−6.1 [43]	2.9 (3.6)	7.0 [44]	3.38 ± 0.05
DMAC-TRZ [10-(4-(4,6-diphenyl-1,3,5-triazin-2-yl)phenyl) -9,9-dimethyl-9,10-dihydroacridine]	−5.3 [37], −5.49 [26]	2.4 (2.7)	2.01 [45]	3.07 ± 0.06

[a]From UPS experiments. Onset energy with respect to the vacuum level, defined conventionally [46] by extrapolating the tangent through the low-binding-energy inflection point of the HOMO peak to the background intensity level. Due to electronic and vibronic relaxation effects, energetic disorder, and the surface sensitivity, E_{IE} is, in general, not equal to $-E_{HOMO}$ [17,47].
[b]Highest-energy peak (onset) energy of the PL spectra, obtained for the devices studied. Due to vibronic effects, light-outcoupling effects, and excitonic disorder, the peak or onset energies are, in general, not equal to the average adiabatic singlet energy.
[c]From capacitance measurements. See Secs. IV C and S6 in the Supplemental Material [28].
[d]α-MADN is also called α,α-MADN, or MAD-1N. β-MADN is also called β,β-MADN, or MADN.

intensity. For none of the devices was a change of the spectral shape observed (see Fig. S9 in Sec. S7 of the Supplemental Material [28]). We note that the results for mCP are less reliable because of a small overlap of the PL spectrum with the 337 nm laser wavelength. The $\eta_{PL}(V)$ curve that is shown is based on the part of the PL spectrum above 340 nm.

Within the voltage range studied, the decrease of the relative PL efficiency is largest for the TADF-emitter DMAC-TRZ, to about 27% at −50 V. Also, for TPBi, a quite large decrease is found, to about 57% at −50 V. For all other materials, the decrease is much smaller, down to only ≈10% for α-MADN, β-MADN, and TCTA. The shape of the curves is seen to be strongly material dependent. For DMAC-TRZ, a significant decrease of the PL efficiency sets in beyond approximately −20 V (field $F = 1 \times 10^8$ V/m), whereas for NPB, TCTA, CBP, mCP, and TPBi, the decrease already sets in almost immediately, at very small voltages. For the two isomers of MADN, the shape of the PL curves is somewhat

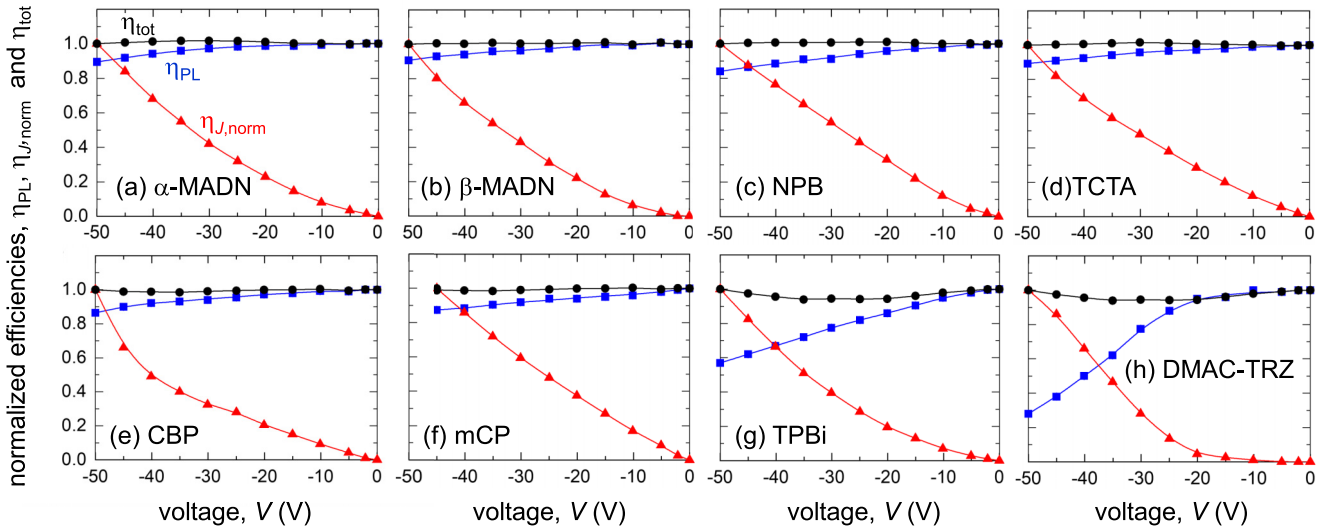

FIG. 6. Voltage dependence of the results of the FID experiments for the materials studied in this work. Blue squares: normalized PL efficiency, $\eta_{PL}(V)$. Red triangles: normalized photocurrent yield, $\eta_{J,norm}(V)$. Black filled circles: normalized total yield $\eta_{tot}(V)$, defined by Eq. (6).

intermediate. For NPB devices, the thickness dependence of the PL efficiency was studied. For devices in the range 100–300 nm, no significant difference was found (see Fig. S10(a) in Sec. S8 of the Supplemental Material [28]). For these devices, the spectral shape shows a wavelength dependence (see Fig. S10(b) in Sec. S8 of the Supplemental Material [28]). Such an effect is expected in view of the thickness dependence of the light-outcoupling efficiency. By focusing on devices with relatively thick (200 nm) organic semiconductor layers, the FID curves are expected to be relatively insensitive to microcavity effects. However, refined analyses should include such effects.

For all materials, the photocurrent density increases with increasing reverse-bias voltage. The red triangles in Fig. 6 show the normalized photocurrent yield, defined as $\eta_{J,\mathrm{norm}}(V) \equiv \bar{J}_{\mathrm{phot}}(V)/\bar{J}_{\mathrm{phot}}(-50\,\mathrm{V})$, i.e., the time-averaged photocurrent density, normalized to the value at −50 V. The time-resolved photocurrent density peaks are asymmetric, with a fast immediate rise after light absorption and a slow decay, typically on a timescale of the order of 10 μs. For a series of experiments with equal illumination intensities and equal optical spot areas (1 mm^2), the peak photocurrent density at −50 V was found to vary from ∼160 $\mathrm{A/m}^2$ for the CBP devices to ∼1000 $\mathrm{A/m}^2$ for the TPBi devices. In order to avoid breakdown, the experiments for mCP were carried out up to −30/V, at which a peak photocurrent density of ∼90 $\mathrm{A/m}^2$ was found. See Fig. S11 in Sec. S9 of the Supplemental Material [28].

When all excitons that are dissociated would contribute to the photocurrent, the normalized total yield

$$\eta_{\mathrm{tot}}(V) \equiv \eta_{\mathrm{PL}}(V) + [1 - \eta_{\mathrm{PL}}(-50\,\mathrm{V})]\eta_{J,\mathrm{norm}}(V) \qquad (6)$$

would be expected to be equal to unity for all voltages. In Fig. 6, this function is given by black filled circles. For all materials, it may be seen that the total yield is indeed, to a fair approximation, conserved. The deviation is largest, about 10%, for TPBi. We regard such a deviation as an indication of the occurrence of nonradiative decay of field-induced charge-transfer (CT) state excitons.

E. Analysis using KMC simulations with a fixed set of material parameters

Figure 7 shows the electric-field (F)-dependent $\eta_{\mathrm{PL}}(F)$ curves for all materials, together with the results of four sets of 3D-KMC simulations (dashed curves) that have been obtained using the methodology that was developed in paper I [1]. We refer to that paper for the technical details.

The black long-dashed curves are simulation results for three values of the singlet-exciton binding energy, taken from Fig. 5(a) of paper I [1]. The simulations have been carried out using a set of other parameters that we regard as characteristic for many small-molecule fluorescent emitters and hole-transporting materials such as used in OLEDs: an average intersite distance (a) of 1 nm, a hopping attempt rate to the first neighbor molecules (ν_1) of 3.3×10^{10} s^{-1}, a radiative lifetime (τ_{rad}) of 10^{-8} s, a relative dielectric permittivity (ε_{r}) of 3, Gaussian electronic and excitonic disorder with widths of 0.10 eV and 0.05 eV, respectively, and wave-function decay lengths for hole, electrons, and excitons of 0.3 nm. The

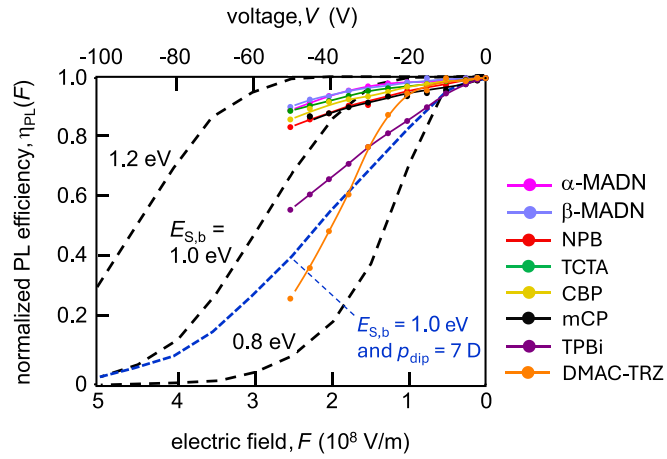

FIG. 7. Full curves and symbols: field dependence of the normalized PL efficiency, $\eta_{\mathrm{PL}}(F)$, obtained from FID experiments for all materials. Dashed curves: $\eta_{\mathrm{PL}}(F)$ obtained from 3D-KMC simulations for the parameter set that has been discussed in Sec. IIE, for materials without static dipoles (black long-dashed curves) and with randomly oriented 7 D static dipole moments (blue short-dashed curves).

simulations were carried out for correlation model 2, discussed in Sec. 2B of paper I [1]: (i) no correlation was assumed between the local HOMO and LUMO (lowest unoccupied molecular orbital) state energies, and (ii) no correlation was assumed between the local singlet energies and the local HOMO-LUMO gap energy.

Figure 7 shows that for all materials studied, except for TPBi and DMAC-TRZ, simulations using the set of selected parameters suggest that $E_{\mathrm{S,b}}$ is larger than 1.0 eV. Estimating an upper limit is presently difficult due to the occurrence of dielectric breakdown well before the $F_{1/2}$ field (50% efficiency loss) has been reached. The figure also shows that the PL intensity decays at low fields more strongly than as expected from the simulations. We regard that as an indication that broadening due to electronic or excitonic disorder plays a role (see Fig. 5(b) of paper I [1]). Positional disorder was not included in the simulations that were presented in paper I [1] and might also contribute to this effect.

For TPBi, the presence of large dipole moments (7 D on average, from first-principles simulations in Ref. [44]) leads to strongly enhanced electronic disorder. As shown in Fig. 5(b) of paper I [1], a decrease of the PL efficiency and a decrease of the steepness of the curves around the $F_{1/2}$ field is expected, similar to the effect of increasing the energetic disorder from 0.10 to 0.15 eV. Such an effect is indeed observed. The blue short-dashed curve in Fig. 7 shows the model result for a value of $E_{\mathrm{S,b}}$ of 1.0 eV.

For DMAC-TRZ, the shape of the experimental FID curve (see Fig. 7) is quite similar to the shape that would be expected from the simulation results for an exciton binding energy of about 0.9 eV. However, for TADF emitters, the analysis is complicated by the occurrence of a delayed contribution to the emission. Whereas, for evaporation-deposited neat films of DMAC-TRZ, the prompt radiative lifetime of 29 ns [50] is of the same order of magnitude as the value of 10 ns that was assumed in the simulations, about half of the emission

TABLE V. Parameter values that have been adapted when refining the 3D-KMC simulations of FID of devices based on α-MADN and β-MADN, as well as the default values. A full overview of the default values is given in Table I of paper I [1]. The simulation results are shown in Fig. 8.

Parameter	Default value	α-MADN	β-MADN
τ_{eff} (ns)	10	0.45[a]	0.30[a]
σ_{exc} (eV)	0.05	0.05[b]	0.07[b]
ε_{r}	3	3.2[c]	3.12[c]
R_{F} (nm)	0	1.5[d]	1.35[d]
σ_{h} (eV)	0.10	0.10[d]	0.13[d]
σ_{e} (eV)	0.10	0.14[d]	0.19[d]

[a] $\tau_{\text{eff}} = (\eta_{\text{PL}}^{\text{neat-film}}/\eta_{\text{PL}}^{\text{blend}})\tau_{\text{blend}}$, using neat film and 5 mol% blend data from Table II.
[b] From Table III.
[c] From Table IV.
[d] From the spectral overlap of film absorption and emission spectra, with $\eta_{\text{PL}} = 0.4$ (from Table II) and assuming a refractive index $n_{\text{refr}} = 1.95$.

is due to the delayed component, with an average lifetime approximately 3 μs [50]. Taking this delayed contribution into account will lead to a larger estimated value of the singlet binding energy, as may be seen from the sensitivity analysis that was given in Fig. 5(c) of paper I [1]. We leave such a refined analysis to future work. For all materials, simulations using material-specific parameters would be needed to obtain more accurate values of the exciton binding energy.

F. Analysis using KMC simulations with material-specific parameters

In this section, we refine the analysis of the FID results for the two isomers of MADN using material-specific experimental and theoretical parameters that have been presented in this paper and in paper II [8], respectively. Table V gives an overview of the adapted parameter values, in the order of the discussion on the sensitivity given below. As in the previous section, no HOMO-LUMO correlation or correlation between the local HOMO-LUMO gap and the local exciton energy is assumed ($\rho_1 = 0$ and $\rho_2 = 0$; see Fig. 1(b) of paper I [1]).

Figure 8 shows the effect of these adaptations on the 3D-KMC simulation results for α-MADN and β-MADN, and a comparison with the experimental results. Figure 8(a) shows intermediate simulation results for α-MADN, for $E_{\text{S,b}} = 1.0$ eV. The black thick and long-dashed thick curve gives the 3D-KMC result using the default parameter set. The magenta thick and full curve gives the final result after including all adaptations given in Table V. The comparison in Fig. 8(b) between the experimental results with simulation results for the complete material-specific parameter set and for three values of $E_{\text{S,b}}$ shows that the data are indeed best described using $E_{\text{S,b}} \approx 1$ eV. This value is 0.1 eV smaller than the value that was estimated in Sec. IV E using the default set of simulations parameters. The various curves in Fig. 8(a) show the sensitivity to material-specific parameters. The first adaptation concerns the effect of concentration quenching,

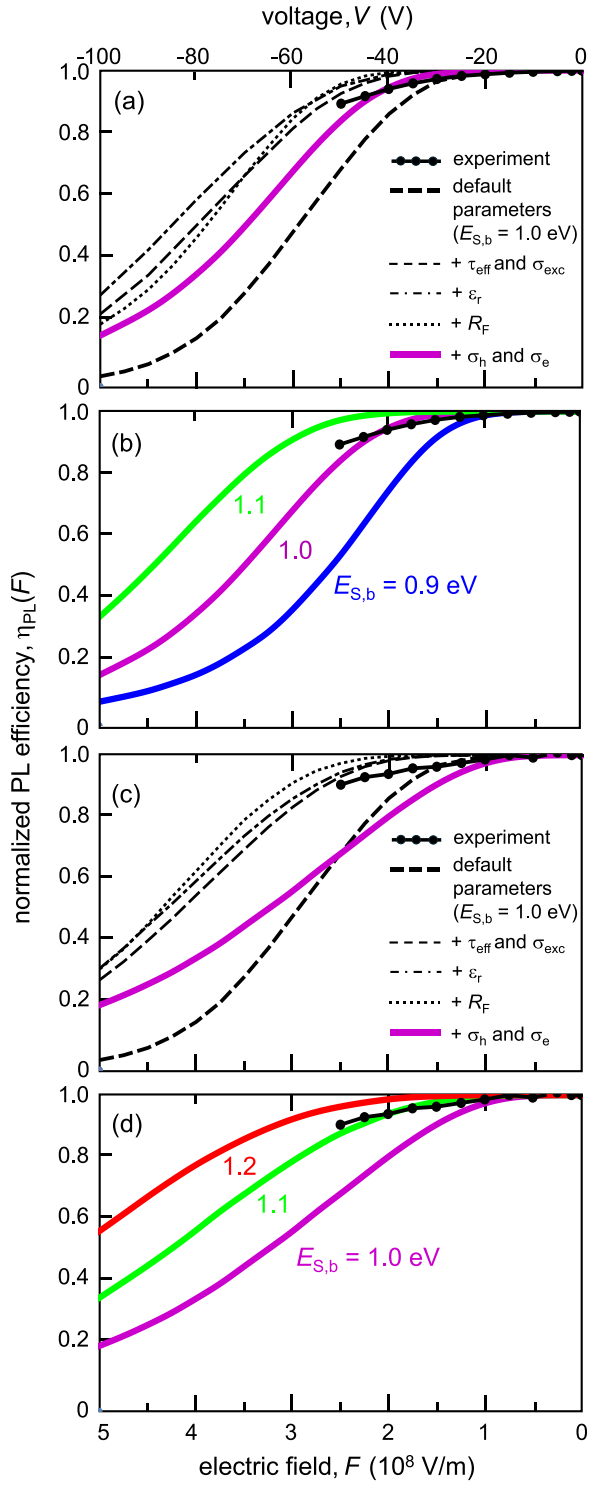

FIG. 8. Analysis of the experimental field dependence of the normalized PL efficiency $\eta_{\text{PL}}(F)$ of (a),(b) α-MADN and (c),(d) β-MADN devices (black full curves and symbols) using 3D-KMC simulations. The simulation curves in (a) and (c) have been obtained for $E_{\text{S,b}} = 1.0$ eV and with stepwise refined other material-specific parameters. The parameters are given in Table V. The various dashed curves give intermediate results, specified in the figure captions and in the text of Sec. IV F. (b) and (d) show the results of a final analysis step, for various values of $E_{\text{S,b}}$ using otherwise material-specific parameters.

which in Sec. III B was found to lead to a strong reduction of the PL efficiency in neat films and to a reduced effective lifetime. The thin long-dashed curve gives the resulting adapted efficiency curve, which has been obtained by reducing the lifetime by a factor $\eta_{\mathrm{PL}}^{\mathrm{neat-film}}/\eta_{\mathrm{PL}}^{\mathrm{blend}}$ with respect to the value in the 5 mol% blends in UGH2, leading to $\tau_{\mathrm{rad,eff}} \approx 0.45$ ns. A comparison with the default curve shows that the effect is significant. We note that ideally, a KMC model should describe the effects of exciton diffusion to quenching sites. As we have insufficient information about the nature and distribution of the quenching sites, we have simplified the analysis by focusing on the resulting decrease of the effective lifetime. The dash-dotted and dotted simulated FID curves in Fig. 8(a) have been obtained by sequentially adding the adapted values of ε_{r} and R_{F}, respectively. The figure shows that the effect of these adaptations is relatively small. The observed effects are found to be consistent with the sensitivity analysis that has been given in paper I [1]. As a last step, the effect of the relatively large disorder energy of the LUMO states, 0.14 eV, has been included (magenta curve). Consistent with the results shown in paper I [1], enhanced energetic disorder is seen to make field-induced dissociation easier. A small adaptation that has not been included in the analysis is the effect of the intersite distance a. Quantum-chemical simulations (see paper II [8]) yield values of 0.869 and 0.876 nm for α-MADN and β-MADN, respectively, instead of the default value of 1 nm. For both isomers, the correction to $E_{\mathrm{S,b}}$ is only about $+0.01$ eV.

Figures 8(c) and 8(d) give a similar comparison of the experimental results with 3D-KMC simulations results for β-MADN. The most important adaptations, to the effective lifetime and to the electron and hole disorder energies, lead to opposite and partially cancelling effects on the PL efficiency curves. The best-fit value of $E_{\mathrm{S,b}}$ is not significantly different from the value that would be obtained using the set of default parameters that is given in Table V, and remains approximately 1.1 eV.

We remark that a potentially important additional refinement would be the use of material- and charge-carrier-specific values of the hopping attempt rate ν_1. From Eq. (17) and Table II in paper I [1], an error of a factor of 10 in the values of ν_1 for electrons and holes is expected to lead to an error of about 0.07 eV in $E_{\mathrm{S,b}}$. In Sec. S10 of the Supplemental Material [28], we argue, using results of hole transport studies of thin films, that such experiments suggest only a marginal correction to the value of $E_{\mathrm{S,b}}$ that has been obtained above for α-MADN, and a correction of about 0.04 eV for β-MADN. From a sensitivity study, we find that for both isomers, deviations in ν_1 for electron hopping by a factor in the range 0.1 to 10 with respect to the default value would lead to deviations of the binding energy of, at most, ± 0.05 eV. For β-MADN, these findings lead thus to an upward shift of $E_{\mathrm{S,b}}$ to about 1.14 eV. And for both isomers, these findings lead to an increase of the uncertainty margin, which is estimated at ± 0.10 eV.

We also remark that after refining the analysis of the FID experiments by using material-specific parameter values, the simulation results do not yet provide a fully satisfactory fit to the experimental curves (see Fig. 8). A similar discrepancy is observed for various other materials (see Fig. 7). As a first possible explanation, we may consider a field dependence of the nonradiative decay rate of singlet excitons on the MADN emitters or of the field-induced CT states. However, we find from an analysis given in Sec. S10 of the Supplemental Material [28] that such an effect could play a role, in general, but is less likely for the two isomers of MADN. A second possible explanation would be the presence of a larger-than-expected fraction of molecular sites with a very small exciton binding energy, e.g., due to aggregate formation. We cannot present a refined analysis of the FID curves that includes such an effect. However, we expect that the resulting additional uncertainty of the values of $E_{\mathrm{exc,b}}$ is only about ± 0.05 eV.

V. SUMMARY, CONCLUSIONS, AND OUTLOOK

In this paper, we have proposed the use of the combined results of UPS experiments, optical spectroscopy, and field-induced dissociation experiments to obtain the electron affinity of disordered organic semiconductors, using Eq. (1), and have applied this approach to the two isomers of MADN. Whereas the adiabatic values of E_{IE} have been obtained from the simulation-assisted analysis of UPS experiments that has been presented in Ref. [17], adiabatic values of E_{S} and $E_{\mathrm{S,b}}$ have been obtained in this work from analyses of optical absorption and emission experiments and from field-induced dissociation experiments. Table VI gives an overview of all experimental results and also gives a comparison with the theoretical results from quantum-chemical simulations that have been presented in paper II [8]. The table shows that the experimental values of E_{S} and $E_{\mathrm{S,b}}$ agree well with the theoretical work in paper II [8], with deviations of about 0.1 eV for the adiabatic singlet energies and of up to about 0.1 eV for the exciton binding energies. The finally resulting experimental electron affinities are, within the uncertainty margins that have been indicated, consistent with the theoretical values that have been obtained in paper II [8]. These experimental values are also very close to the onset values that have been obtained in paper II [8] from LEIPS experiments (1.85 and 1.76 eV for α-MADN and β-MADN, respectively). However, as stated in paper II [8], this agreement must be regarded as somewhat fortuitous, in view of the partially compensating effects that determine the difference between the onset energy and the bulk adiabatic LUMO energy.

This work shows that obtaining exciton binding energies with an accuracy of about 0.10–0.15 eV from FID experiments is feasible, in agreement with the analysis given in paper I [1]. However, the accuracy with which, using Eq. (1), the value of E_{EA} can be deduced is less good, due to the additional uncertainty of the experimental values of the ionization energy and the singlet energy. The table shows that for these materials, the theoretical workflow provides the electron affinity with a smaller uncertainty than the experimental approach. Future applications of the experimental and theoretical workflows to more materials are expected to help refine their analyses, thereby reducing the uncertainties in all quantities that enter Table VI. We have also carried out the FID experiments for six other often-used organic semiconductor materials and find, from simulations using a default parameter set, that for these materials, the exciton binding energy is typically 1.0–1.2 eV. For the two isomers of MADN,

TABLE VI. Comparison of the experimental values of the ionization energy E_{IE}, the optical gap (singlet) energy E_S, the singlet-exciton binding energy $E_{S,b}$ and the electron affinity E_{EA} for α-MADN and β-MADN with the theoretical values that are given in paper II [8] and in Table I. The energies are distribution-averaged adiabatic bulk values, expressed in units eV. The italicized energies are the main results of this work.

	α-MADN		β-MADN	
	Experiment	Theory	Experiment	Theory
E_{IE}	5.91 ± 0.10[a]	5.91 ± 0.05[b]	5.87 ± 0.10[a]	5.89 ± 0.05[b]
E_S	3.04 ± 0.03[c]	2.96 ± 0.04[d]	2.98 ± 0.03[c]	2.90 ± 0.04[d]
$E_{S,b}$	1.00 ± 0.10[e]	1.12 ± 0.14[f]	1.14 ± 0.10[e]	1.16 ± 0.12[f]
		1.02 ± 0.14[g]		1.10 ± 0.12[g]
E_{EA}	*1.83 ± 0.24*[h]	1.83 ± 0.13[i]	*1.75 ± 0.24*[h]	1.83 ± 0.14[i]

[a]From UPS, analyzed using quantum-chemical theory [17].
[b]From Ref. [17].
[c]Adiabatic singlet energy, defined in Eq. (2), from Table III.
[d]From the calculated bulk 0-0 peak energy for absorption, $E_{0-0,A}$, in paper II [8] and the measured Stokes shift ΔE_S (see Table III), using $E_S = E_{0-0,A} - \Delta E_S/2$.
[e]From an analysis of FID experiments using KMC simulations with material-specific parameters, in Sec. IV F.
[f]From paper II [8], using Eq. (1) with the values of E_{IE} and E_{EA} that are given in this table.
[g]From paper II [8], using Eq. (1) with the value of $E_{gap} \equiv E_{IE} - E_{EA}$ that has been obtained directly from the distribution of gap energies across the film thickness, as obtained from Fig. 8 in paper II [8]. This procedure avoids possible errors in E_{IE} and E_{EA}. These energies vary across the film thickness due to an internal electrostatic field, and are, in paper II [8], obtained by extrapolation to the vacuum surface.
[h]Obtained using Eq. (1), with an uncertainty that is taken equal to the sum of the uncertainties of E_{IE}, E_S, and $E_{S,b}$.
[i]From paper II [8], using the methodology for obtaining $E_{S,b}$ that has been described under footnote "g" in paper II [8].

an analysis of the field dependence of the PL efficiency using KMC simulations that are based on default parameters already provides a good first estimate of the binding energy. However, the relatively small sensitivity to material-specific parameters was found to be due to partially compensating errors. Carrying out refined analyses with 3D-KMC simulations will help improve the accuracy of the values of $E_{S,b}$ that are determined, in particular in special cases. Examples are materials with large static dipole moments, such as TPBi, or TADF materials with a relatively large radiative lifetime, such as DMAC-TRZ.

We regard the simulation-assisted method for obtaining exciton binding energies from FID measurements that has been presented in this paper as a promising tool when studying the device physics of organic electronic devices such as OLEDs. As suggested by Fig. 7, it will be of interest to apply the method systematically to materials with varying static dipole moments and to TADF emitter materials, within which FID has been observed to already occur at smaller fields than within materials with localized excitons and only small static dipole moments. It will also be of interest to refine the analysis of the FID experiments by varying the organic layer thickness, by carrying out time-resolved studies of the PL intensity and the photocurrent, or by studying FID in blend systems. Studies for binary or ternary systems are expected to help elucidate the separate roles of field-induced electron and hole transfer upon dissociation. The theoretical analysis of FID experiments can be refined by including the effects of positional and orientational disorder and the photophysics of the field-induced charge-transfer states. Further studying the mechanism of the observed dielectric breakdown at high voltages, where charge transfer to less localized (HOMO-1) or (LUMO+1) states possibly occurs, will be relevant to emerging applications of high-voltage organic electronic devices showing large-bandwidth emission [16,54] or amplified stimulated emission [55,56].

ACKNOWLEDGMENTS

This project was funded by the EU Horizon 2020 research and innovation program under the Marie Skłodowska-Curie grant agreement TADFlife (Project No. 812872) and by the project "Suppressing Exciton Quenching in OLEDs: an Integrated Approach" (SEQUOIA, Project No. 18975) of the research program "Open Technology" of the Netherlands Organisation for Scientific Research (NWO). The authors thank Dr. M.-H. Ho (Apple Research) for sharing information on charge-transport measurements of the two isomers of MADN.

DATA AVAILABILITY

The data that support the findings of this article are openly available [57].

[1] E. J. de Jong, S. Gottardi, H. van Eersel, and R. Coehoorn, companion paper, Electron affinity and binding energy of excitons in disordered organic semiconductors. I. Simulation-assisted analysis of field-induced exciton dissociation experiments, Phys. Rev. B **112**, 224202 (2025).
[2] C. Wu, Y. Hirose, H. Sirringhaus, and A. Kahn, Electron-hole interaction energy in the organic molecular semiconductor ptcda, Chem. Phys. Lett. **272**, 43 (1997).
[3] I. G. Hill, A. Kahn, J. Cornil, D. A. dos Santos, and J. L. Bredas, Occupied and unoccupied electronic levels in organic π-conjugated molecules: comparison between experiment and theory, Chem. Phys. Lett. **317**, 444 (2000).
[4] S. Krause, M. B. Casu, A. Schöll, and E. Umbach, Determination of transport levels of organic semiconductors by UPS and IPS, New J. Phys. **10**, 085001 (2008).
[5] H. Yoshida, Near-ultraviolet inverse photoemission spectroscopy using ultra-low energy electrons, Chem. Phys. Lett. **539-540**, 180 (2012).
[6] H. Yoshida and K. Yoshizaki, Electron affinities of organic materials used for organic light-emitting diodes: A low-energy inverse photoemission study, Org. Electron. **20**, 24 (2015).
[7] H. Yoshida, K. Yamada, J. Tsutsumi, and N. Sato, Complete description of ionization energy and electron affinity in organic solids: Determining contributions from electronic polarization,

energy band dispersion, and molecular orientation, Phys. Rev. B **92**, 075145 (2015).

[8] G. Tirimbò, O. Nagaoka, S. Fukushima, C. van Hoesel, H. Yoshida, R. Coehoorn, and B. Baumeier, companion paper, Electron affinity and binding energy of excitons in disordered organic semiconductors. II. First-principles simulations and inverse photoemission studies for MADN, Phys. Rev. B **112**, 224203 (2025).

[9] M.-T. Lee, H.-H. Chen, C.-H. Liao, C.-H. Tsai, and C. H. Chen, Stable styrylamine-doped blue organic electroluminescent device based on 2-methyl-9, 10-di (2-naphthyl) anthracene, Appl. Phys. Lett. **85**, 3301 (2004).

[10] M.-T. Lee, C.-H. Liao, C.-H. Tsai, and C. H. Chen, Highly efficient, deep-blue doped organic light-emitting devices, Adv. Mater. **17**, 2493 (2005).

[11] C.-H. Liao, M.-T. Lee, C.-H. Tsai, and C. H. Chen, Highly efficient blue organic light-emitting devices incorporating a composite hole transport layer, Appl. Phys. Lett. **86**, 203507 (2005).

[12] M.-H. Ho, Y.-S. Wu, S.-W. Wen, M.-T. Lee, T.-M. Chen, C. H. Chen, K.-C. Kwok, S.-K. So, K.-T. Yeung, Y.-K. Cheng *et al.*, Highly efficient deep blue organic electroluminescent device based on 1-methyl-9, 10-di (1-naphthyl) anthracene, Appl. Phys. Lett. **89**, 252903 (2006).

[13] M.-H. Ho, M.-Y. Liu, K.-H. Lin, C. H. Chen, and C. W. Tang, 39.2: Efficient single-layer small molecule blue OLEDs based on a multifunctional bipolar transport material, in *SID Symposium Digest of Technical Papers*, Vol. 41 (Blackwell Publishing Ltd., Oxford, UK, 2010), pp. 552–555.

[14] M.-H. Ho, B. Balaganesan, and C. H. Chen, Blue fluorescence and bipolar transport materials based on anthracene and their application in OLEDs, Isr. J. Chem. **52**, 484 (2012).

[15] J. Huang, J.-H. Su, and H. Tian, The development of anthracene derivatives for organic light-emitting diodes, J. Mater. Chem. **22**, 10977 (2012).

[16] K. Yoshida, P. P. Manousiadis, R. Bian, Z. Chen, C. Murawski, M. C. Gather, H. Haas, G. A. Turnbull, and I. D. Samuel, 245 Mhz bandwidth organic light-emitting diodes used in a gigabit optical wireless data link, Nat. Commun. **11**, 1171 (2020).

[17] G. Tirimbò, X. de Vries, C. H. L. Weijtens, P. A. Bobbert, T. Neumann, R. Coehoorn, and B. Baumeier, Quantitative predictions of photoelectron spectra in amorphous molecular solids from multiscale quasiparticle embedding, Phys. Rev. B **101**, 035402 (2020).

[18] S.-W. Wen, M.-T. Lee, and C. H. Chen, Recent development of blue fluorescent OLED materials and devices, J. Display Technol. **1**, 90 (2005).

[19] S.-K. Kim, B. Yang, Y. Ma, J.-H. Lee, and J.-W. Park, Exceedingly efficient deep-blue electroluminescence from new anthracenes obtained using rational molecular design, J. Mater. Chem. **18**, 3376 (2008).

[20] T. Zheng and W. C. Choy, High-efficiency blue fluorescent organic light emitting devices based on double emission layers, J. Phys. D: Appl. Phys. **41**, 055103 (2008).

[21] Y.-H. Kim, J. H. Seo, G. W. Hyung, S. Y. Lee, D. H. Ryu, S. J. Chae, S. S. Shin, Y. K. Kim, and W. Y. Kim, Fabrication of white organic light-emitting diodes using two complementary color methods, Mol. Cryst. Liq. Cryst. **510**, 282 (2009).

[22] M. H. Park, Y. S. Kim, S. Lee, and K. H. Koh, Optical properties of a blue light-emitting host material, MADN, New Physics: Sae Mulli **57**, 133 (2008).

[23] K. H. Lee, S. O. Kim, J. N. You, S. Kang, J. Y. Lee, K. S. Yook, S. O. Jeon, J. Y. Lee, and S. S. Yoon, Tert-butylated spirofluorene derivatives with arylamine groups for highly efficient blue organic light emitting diodes, J. Mater. Chem. **22**, 5145 (2012).

[24] N. Xiang, X. Huang, Z. Xia, G. Tian, J. Huang, Q. Wang, and J. Su, Synthesis and properties of novel 9, 10-di (naphthalen-2-yl) anthracene derivatives, Tetrah. Lett. **57**, 1847 (2016).

[25] X. Ren, J. Li, R. J. Holmes, P. I. Djurovich, S. R. Forrest, and M. E. Thompson, Ultrahigh energy gap hosts in deep blue organic electrophosphorescent devices, Chem. Mater. **16**, 4743 (2004).

[26] C. H. L. Weijtens (unpublished).

[27] M. de Jong, L. Seijo, A. Meijerink, and F. T. Rabouw, Resolving the ambiguity in the relation between Stokes shift and Huang–Rhys parameter, Phys. Chem. Chem. Phys. **17**, 16959 (2015).

[28] See Supplemental Material at http://link.aps.org/supplemental/10.1103/kcl9-54vq for the overviews of the wavelength dependent absorption and photoluminescence (PL) spectra and of time-resolved PL experiments for the two isomers of MADN, Franck-Condon analyses of the PL spectra, current-voltage characteristics, capacitance-frequency curves, voltage dependent PL spectra and the time-resolved photocurrent density for all devices for which FID experiments have been carried out, results of a study of the thickness dependence of FID curves for NPB-based devices, results of a study of the hole hopping attempt rate in films of the two isomers of MADN, and an analysis of the possible effect of field-dependent nonradiative decay on the results of FID experiments, which includes Refs. [12,13,32,43,58–66].

[29] M. Pope and C. E. Swenberg, *Electronic Processes in Organic Crystals and Polymers* (Oxford University Press, New York, Oxford, 1999).

[30] T. Serevičius, R. Komskis, P. Adomėnas, O. Adomėnienė, V. Jankauskas, A. Gruodis, K. Kazlauskas, and S. Juršėnas, Non-symmetric 9, 10-diphenylanthracene-based deep-blue emitters with enhanced charge transport properties, Phys. Chem. Chem. Phys. **16**, 7089 (2014).

[31] S. R. Forrest, *Organic Electronics: Foundations to Applications* (Oxford University Press, New York, 2020).

[32] X. de Vries, P. Friederich, W. Wenzel, R. Coehoorn, and P. A. Bobbert, Full quantum treatment of charge dynamics in amorphous molecular semiconductors, Phys. Rev. B **97**, 075203 (2018).

[33] S. T. Hoffmann, S. Athanasopoulos, D. Beljonne, H. Bässler, and A. Köhler, How do triplets and charges move in disordered organic semiconductors? A Monte Carlo study comprising the equilibrium and nonequilibrium regime, J. Phys. Chem. C **116**, 16371 (2012).

[34] P. K. H. Ho, J.-S. Kim, N. Tessler, and R. H. Friend, Photoluminescence of poly(p-phenylenevinylene)–silica nanocomposites: Evidence for dual emission by Franck-Condon analysis, J. Chem. Phys. **115**, 2709 (2001).

[35] F. Gao, Y. Zhao, and W. Liang, Theoretical studies toward understanding the excited state dynamics of a bichromophoric molecule, J. Chem. Phys. **126**, 224509 (2007).

[36] G. Heimel, M. Daghofer, J. Gierschner, E. J. List, A. C. Grimsdale, K. Müllen, D. Beljonne, J.-L. Brédas, and E. Zojer,

Breakdown of the mirror image symmetry in the optical absorption/emission spectra of oligo(para-phenylene)s, J. Chem. Phys. **122**, 054501 (2005).

[37] W.-L. Tsai, M.-H. Huang, W.-K. Lee, Y.-J. Hsu, K.-C. Pan, Y.-H. Huang, H.-C. Ting, M. Sarma, Y.-Y. Ho, H.-C. Hu *et al.*, A versatile thermally activated delayed fluorescence emitter for both highly efficient doped and non-doped organic light emitting devices, Chem. Commun. **51**, 13662 (2015).

[38] A. Kahn, N. Koch, and W. Gao, Electronic structure and electrical properties of interfaces between metals and π-conjugated molecular films, J. Polym. Sc. B: Polymer Phys. **41**, 2529 (2003).

[39] X. de Vries, P. Friederich, W. Wenzel, R. Coehoorn, and P. A. Bobbert, Triplet exciton diffusion in metalorganic phosphorescent host-guest systems from first principles, Phys. Rev. B **99**, 205201 (2019).

[40] C. H. L. Weijtens (unpublished).

[41] C. Hauenstein, X. De Vries, C. Weijtens, P. Imbrasas, P.-A. Will, S. Lenk, K. Ortstein, S. Reineke, P. Bobbert, R. Coehoorn *et al.*, Suppressing exciton deconfinement and dissociation for efficient thermally activated delayed fluorescence OLEDs, J. Appl. Phys. **130**, 155501 (2021).

[42] I. G. Hill and A. Kahn, Energy level alignment at interfaces of organic semiconductor heterostructures, J. Appl. Phys. **84**, 5583 (1998).

[43] R. Coehoorn, X. Lin, C. H. L. Weijtens, S. Gottardi, and H. van Eersel, Three-dimensional modeling of organic light-emitting diodes containing molecules with large electric dipole moments, Phys. Rev. Appl. **16**, 034048 (2021).

[44] P. Friederich, V. Rodin, F. von Wrochem, and W. Wenzel, Built-in potentials induced by molecular order in amorphous organic thin films, ACS Appl. Mater. Interfaces **10**, 1881 (2018).

[45] B. A. Naqvi, M. Schmid, E. Crovini, P. Sahay, T. Naujoks, F. Rodella, Z. Zhang, P. Strohriegl, S. Bräse, E. Zysman-Colman *et al.*, What controls the orientation of TADF emitters? Front. Chem. **8**, 750 (2020).

[46] B. W. D'Andrade, S. Datta, S. R. Forrest, P. Djurovich, E. Polikarpov, and M. E. Thompson, Relationship between the ionization and oxidation potentials of molecular organic semiconductors, Org. Electron. **6**, 11 (2005).

[47] I. Hill, A. Kahn, Z. Soos, and R. Pascal, Jr., Charge-separation energy in films of π-conjugated organic molecules, Chem. Phys. Lett. **327**, 181 (2000).

[48] T.-A. Lin, T. Chatterjee, W.-L. Tsai, W.-K. Lee, M.-J. Wu, M. Jiao, K.-C. Pan, C.-L. Yi, C.-L. Chung, K.-T. Wong *et al.*, Sky-blue organic light emitting diode with 37% external quantum efficiency using thermally activated delayed fluorescence from spiroacridine-triazine hybrid, Adv. Mater. **28**, 6976 (2016).

[49] M. Y. Wong and E. Zysman-Colman, Purely organic thermally activated delayed fluorescence materials for organic light-emitting diodes, Adv. Mater. **29**, 1605444 (2017).

[50] K. Stavrou, L. G. Franca, and A. P. Monkman, Photophysics of TADF guest-host systems: Introducing the idea of hosting potential, ACS Appl. Electr. Mater. **2**, 2868 (2020).

[51] R. Dhali, D. A. P. Huu, F. Bertocchi, C. Sissa, F. Terenziani, and A. Painelli, Understanding TADF: A joint experimental and theoretical study of DMAC-TRZ, Phys. Chem. Chem. Phys. **23**, 378 (2021).

[52] C. Murawski, K. Leo, and M. C. Gather, Efficiency roll-off in organic light-emitting diodes, Adv. Mater. **25**, 6801 (2013).

[53] X. de Vries and R. Coehoorn, Vibrational mode contribution to the dielectric permittivity of disordered small-molecule organic semiconductors, Phys. Rev. Mater. **4**, 085602 (2020).

[54] D. Lenstra, A. P. A. Fischer, A. Ouirimi, A. C. Chime, N. Loganathan, and M. Chakaroun, Ultra-short optical pulse generation in micro oleds and the perspective of lasing, J. Opt. **24**, 034007 (2022).

[55] A. S. Sandanayaka, T. Matsushima, F. Bencheikh, S. Terakawa, W. J. Potscavage, C. Qin, T. Fujihara, K. Goushi, J.-C. Ribierre, and C. Adachi, Indication of current-injection lasing from an organic semiconductor, Appl. Phys. Expr. **12**, 061010 (2019).

[56] K. Yoshida, J. Gong, A. L. Kanibolotsky, P. J. Skabara, G. A. Turnbull, and I. D. W. Samuel, Electrically driven organic laser using integrated OLED pumping, Nature (London) **621**, 746 (2023).

[57] E. J. de Jong, N. G. de Rooij, W. F. M. van Geel, C. Hauenstein, H. Tomita, G. Tirimbò, M. Berghuis, S. Fukushima, S. Gottardi, B. Baumeier, H. Yoshida, and R. Coehoorn, Data underlying publication "Electron affinity and binding energy of excitons in disordered organic semiconductors. III. Multimethod study for films of the blue fluorescent emitter MADN", 4TU.ResearchData (2025), 10.4121/d320a48b-aed4-49c3-9885-82cbac8ffe5d.

[58] J. C. de Mello, H. F. Wittmann, and R. H. Friend, An improved experimental determination of external photoluminescence quantum efficiency, Adv. Mater. **9**, 230 (1997).

[59] H. C. F. Martens, H. B. Brom, and P. W. M. Blom, Frequency-dependent electrical response of holes in poly (p-phenylene vinylene), Phys. Rev. B **60**, R8489 (1999).

[60] H. van Eersel, P. Bobbert, R. Janssen, and R. Coehoorn, Monte Carlo study of efficiency roll-off of phosphorescent organic light-emitting diodes: Evidence for dominant role of triplet-polaron quenching, Appl. Phys. Lett. **105**, 143303 (2014).

[61] S. Gottardi, M. Barbry, R. Coehoorn, and H. van Eersel, Efficiency loss processes in hyperfluorescent OLEDs: A kinetic Monte Carlo study, Appl. Phys. Lett. **114**, 073301 (2019).

[62] A. Ligthart, T. D. Nevels, C. H. Weijtens, P. A. Bobbert, and R. Coehoorn, Mechanistic description of the efficiency loss in organic phosphorescent host–guest systems due to triplet-polaron quenching, Org. Electron. **91**, 106058 (2021).

[63] N. B. Kotadiya, A. Mondal, P. W. M. Blom, D. Andrienko, and G.-J. A. H. Wetzelaer, A window to trap-free charge transport in organic semiconducting thin films, Nat. Mater. **18**, 1182 (2019).

[64] N. B. Kotadiya, A. Mondal, S. Xiong, P. W. Blom, D. Andrienko, and G.-J. A. Wetzelaer, Rigorous characterization and predictive modeling of hole transport in amorphous organic semiconductors, Adv. Electr. Mater. **4**, 1800366 (2018).

[65] F. Liu, Y. Su, X. Lin, L. Nian, B. Wu, Q. Niu, H. van Eersel, P. A. Bobbert, R. Coehoorn, and G. Zhou, Image-force-stabilized interfacial dipole layer impedes charge injection into disordered organic semiconductors, Phys. Rev. Appl. **17**, 024003 (2022).

[66] M.-H. Ho (private communication).